ISPRS Journal of Photogrammetry and Remote Sensing 172 (2021) 147–159

Contents lists available at ScienceDirect

ISPRS Journal of Photogrammetry and Remote Sensing

journal homepage: www.elsevier.com/locate/isprsjprs

Digital surface model generation for drifting Arctic sea ice with low-textured surfaces based on drone images

Jae-In Kim [a], Chang-Uk Hyun [a], Hyangsun Han [a,b], Hyun-Cheol Kim [a,*]

[a] Center of RS & GIS, Korea Polar Research Institute (KOPRI), Incheon 21990, Republic of Korea
[b] Department of Geophysics, Kangwon National University, Chuncheon 24341, Republic of Korea

ARTICLE INFO

Keywords:
Sea ice
Digital surface model
Unmanned aerial vehicle
Image matching
Georeferencing
Low-textured surface

ABSTRACT

Arctic sea ice is constantly moving and covered with low-textured surfaces, making it difficult to generate reliable digital surface models (DSMs) from drone images. The movement of sea ice makes georeferencing of DSMs difficult, and the low-textured surfaces of sea ice cause the uncertainty of image matching. This paper proposes a robust method to generate high-quality DSMs for drifting sea ice. To overcome the challenges, the proposed method introduces four improvements to the object-space-based image-matching pipeline: relative georeferencing to recover the horizontality and scale of sea-ice DSMs using a terrestrial light detection and ranging (LiDAR) dataset, match inspection to verify the matched points using several matching constraints, adaptive search-window adjustment to ensure distinct texture information through simple texture analysis, and robust vertical positioning to reduce the matching uncertainty via matching-indicator modeling. Performance evaluations were conducted with drone and LiDAR datasets obtained from a sea-ice campaign using the Korean Icebreaker Research Vessel (IBRV) Araon in the summer of 2017. The experimental results indicated that the proposed method can achieve significant quality enhancements compared with the existing matching method and that all the considerations contributed significantly to the enhancements.

1. Introduction

Arctic sea ice is an important factor affecting global climate change (Kim et al., 2019a; Nolin and Mar, 2019; Vihma, 2014). This is because the bright surfaces of sea ice reflect up to 80% of the incident sunlight back into space, whereas open water caused by ice melting absorbs up to 90% of the sunlight (Eicken et al., 2004; Scharien and Yackel, 2005). Because of this positive ice-albedo feedback, a reduction in the amount of sea ice accelerates global warming (Vinnikov, 1999; Meier et al., 2014; Pistone et al., 2014). Therefore, to evaluate the current status of global warming and predict its future impact, periodic monitoring of the Arctic sea-ice regime is essential.

Sea ice can be characterized according to its concentration, extent, thickness, roughness, etc. (Vinnikov, 1999; Scharien and Yackel 2005; Lang et al., 2017). Although sea ice is widely distributed throughout the Arctic Ocean, these parameters can be derived and analyzed from various satellite data with wide coverage and repeatability (Karvonen et al., 2012). However, there are many difficulties in the development of satellite remote-sensing methods for this purpose. Arctic clouds and polar nights limit the use of satellite data. It is also difficult to distinguish between clouds, ice, and snow from satellite data. In particular, obtaining field data is the most significant challenge, owing to the limited accessibility to Arctic sea ice (Tschudi et al., 2008; Hong et al., 2018). This makes it difficult to generate various sea-ice products.

As a solution to this limitation, the utilization of manned and unmanned aerial vehicles has recently emerged (Hagen et al., 2014; Divine et al., 2016). These observation platforms enable the acquisition of scientific data without unpredictable dangers on sea ice, such as the threat from wild animals and the collapse of ice. Although this approach may be inaccurate compared with manual field surveys, it can acquire denser and more extensive data, such as mosaic images and digital surface models (DSMs). DSMs are very useful in that they provide topographical information about sea ice. In a previous study, we found that sea-ice roughness estimation models based on synthetic aperture radar (SAR) satellites can be developed using sea-ice DSMs (Han et al., 2020). In addition, Hendricks et al. (2010) reported the importance of sea-ice DSMs for verifying freeboard estimation models based on altimetry satellites. Yitayew et al. (2018) tried to verify the topographical information of sea ice derived from interferometric SAR data with height profiles obtained from helicopter-borne measurements.

* Corresponding author.
E-mail addresses: jikim0312@kopri.re.kr (J.-I. Kim), chyun@kopri.re.kr (C.-U. Hyun), hyangsun@kangwon.ac.kr (H. Han), kimhc@kopri.re.kr (H.-C. Kim).

https://doi.org/10.1016/j.isprsjprs.2020.12.008
Received 10 August 2020; Received in revised form 14 November 2020; Accepted 14 December 2020
Available online 31 December 2020

These studies suggest that satellite remote-sensing methods for monitoring sea ice can be established and verified reliably using high-resolution sea-ice DSMs.

However, despite the high utility of sea-ice DSMs, related studies are rare. The reason is associated with the inherent characteristics of sea ice. First, sea ice moves constantly, which makes georeferencing of DSMs difficult. In general, georeferencing can be divided into two methods: indirect and direct. The former method employs the absolute orientation from ground control points (GCPs) surveyed in the field (Toutin, 2004; Turner et al., 2012; Gonçalves and Henriques, 2015; Clapuyt et al., 2016), and the latter is based on observations of a global navigation satellite system and inertial navigation system (GNSS/INS) sensor mounted on an aircraft (Chiang et al., 2012; Turner et al., 2014; Helgesen et al., 2019). Recent advances in hardware and software technologies have significantly improved the performance of both georeferencing methods (Padró et al., 2019). However, the existing methods are limited in that the target objects or areas should not change during the image acquisition.

Second, the surfaces of sea ice are covered with snow and ice. This indicates that sea ice has low-textured surfaces. This lack of texture information is likely to cause outliers in the resulting DSMs, because image matching requires distinct texture information to identify similarities between search windows on acquired images. In other words, low-textured surfaces of sea ice may cause ambiguity problems in comparing similarities between search windows (Veksler, 2003; Yang et al., 2009). The performance of image matching depends on the search-window sizes for collecting surface textures and the matching indicators for quantifying similarities using these textures (Veksler, 2003; Hirschmuller and Scharstein, 2007). Therefore, to reliably generate sea-ice DSMs, the DSM generation should be preceded by the derivation of the optimized matching indicator and search-window size for low-textured surfaces of sea ice. Many studies have been performed on matching indicators. Among the matching indicators that have been developed, the sum of squared differences, normalized cross-correlation (NCC), zero-mean NCC (ZNCC), and mutual information are widely used in many applications (Elboher and Werman, 2013; Hirschmuller and Scharstein, 2009; Pluim et al., 2003). Additionally, performance comparisons between matching indicators have been well established (Banks and Corke, 2001; Hirschmuller and Scharstein, 2009). However, the performance for low-textured surfaces has not been comprehensively investigated. Search windows have also been studied steadily. Search-window methods can be classified into three: multiple-window methods, adaptive-weight methods, and adaptive-window methods. In the multiple-window methods, a matching indicator is evaluated using several predefined windows, and the window with the minimum (or maximum) cost is selected (Fusiello et al., 1997; Kang et al., 2001; Hirschmüller et al., 2002). In the adaptive-weight methods, a matching indicator is evaluated by assigning different weights to each pixel in a fixed-size window (Yoon and Kweon, 2006; Wu et al., 2019). These two types of methods have exhibited good performance—particularly for occlusion areas (i.e. elevation discontinuities)—but are not suitable for low-textured surfaces. On the other hand, the adaptive-window methods are designed for low-textured surfaces (Kanade and Okutomi, 1994; Veksler, 2003; Yang et al., 2009; Zhang et al., 2010; Shi et al., 2016). They segment an image into different areas according to color (or intensity) similarity and allow pixels in the same area to have the same disparity. However, in practice, there can be surfaces with the same color and different elevations. Additionally, it is difficult to clearly determine the criteria for image segmentation. These are critical restrictions, particularly for application to sea-ice surfaces.

For these reasons, this paper aims to solve the problems in georeferencing and image matching, caused by the movement and low-textured surfaces of sea ice. If high-resolution sea-ice DSMs can be reliably constructed, it would be possible not only to develop new sea-ice products from satellite images but also to precisely analyze the topography of sea ice. To this end, in previous studies, we examined the feasibility of mismatch detection in sea-ice DSMs (Kim and Kim, 2018) and also investigated the matching costs optimized for sea-ice surfaces (Kim et al., 2019b). Based on these studies, this paper proposes a robust method to generate high-quality DSMs for drifting sea ice by using drone images. Owing to the low-textured surfaces of sea-ice, the proposed method introduces a coarse-to-fine matching strategy. The initial DSM is produced by image-space-based matching (ISBM), and then the result is improved by object-space-based matching (OSBM). In the OSBM process, the search-window size is variably adjusted for each matching point through texture analysis, and its height is robustly estimated through matching-indicator modeling. The matched points are then verified according to several matching constraints. To consider the movement of sea ice, relative georeferencing is employed in the proposed method. Here, the objective is to ensure the horizontality and scale of sea-ice DSMs on a real-world coordinate system rather than the geolocation accuracy. This is because the absolute orientation of acquired images cannot be accurately achieved due to the constant movement of sea ice. Thus, the georeferencing is conducted by registering the drone DSM created on an arbitrary object-space coordinate system to a reference DSM with the horizontality and scale on a real-world coordinate system. As a reference DSM, we used a terrestrial light detection and ranging (LiDAR) dataset obtained for part of a target area. The performance of the proposed method was evaluated using real datasets collected during an Arctic sea-ice campaign in the summer of 2017. We analyzed the quality of the sea-ice DSMs and the impacts of each of our considerations on the results.

The remainder of this paper is organized as follows. In Section 2, we describe the proposed sea-ice DSM generation method. In Section 3, experimental datasets are presented, and the evaluation results are discussed. Finally, conclusions are drawn in Section 4.

2. Methodology

To resolve the problems caused by the constant movement and low-textured surfaces of sea ice, the proposed method includes four improvements: relative georeferencing, match inspection, adaptive search-window adjustment, and robust vertical positioning. The first improvement is introduced for georeferencing of sea-ice DSMs in response to the movement of sea ice, and the rest are adopted to mitigate the matching uncertainty due to the low-textured surfaces of sea ice. These are organically linked in three processing parts, as shown in Fig. 1. In the first part, matching constraints for match inspection are determined. This process involves relative georeferencing to obtain analysis points with true positions. In the second part, optimal search-window sizes are determined via texture analysis, and an initial DSM is enhanced via match inspection. In the third part, a sea-ice DSM is finally generated via robust vertical positioning. This process is conducted using the derived optimal search windows and the enhanced initial DSM. The match inspection also contributes to this process, by verifying matched points. The corrected sea-ice DSM is finally georeferenced to an absolute ground coordinate system. The initial DSM generation part corresponds to the existing ISBM method. In the following subsections, we first review the general principle of OSBM and then detail the proposed method.

2.1. Principle of OSBM

ISBM methods extract tiepoints between adjacent images and then determine the three-dimensional (3D) positions of the object points corresponding to the tiepoints via space intersection. In contrast, OSBM methods first designate an object space plane (X-Y plane), which is partitioned into regular grids for a target area, and then determine the vertical positions of grids (Zhang et al., 2017; Zhang et al., 2018). Therefore, the key difference between the two types of methods lies in the matching primitive: image features for ISBM and ground features for OSBM.

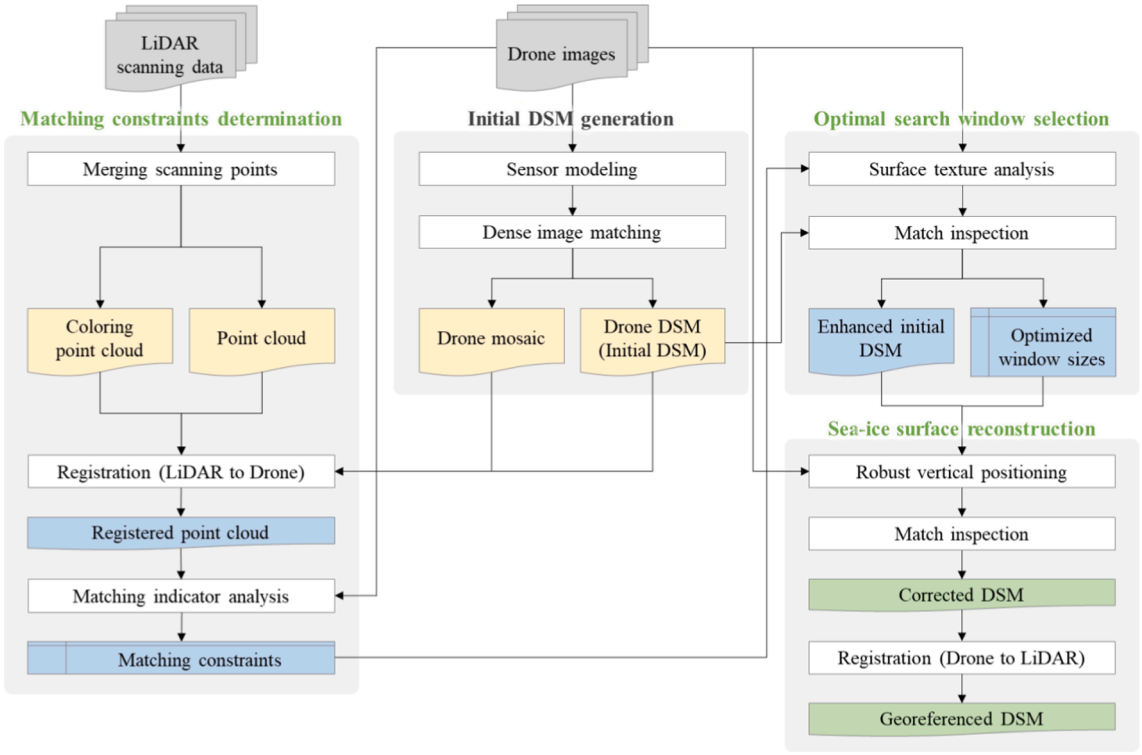

Fig. 1. Workflow of the proposed sea-ice DSM generation method.

As shown in Fig. 2, the vertical position (Z_P) of a DSM grid (X_P, Y_P) is determined by comparing matching-indicator values calculated for different heights ($Z_i = Z_{\min} + i \times \Delta Z$). Search windows in overlapping images are constructed around back-projected image points for a given height (Z_i). Matching-indicator values are then calculated between a reference window and the remaining target windows, and the representative value for the given height is set as the average of the matching-indicator values. Thus, if the vertical position of the DSM grid is correctly determined, the matching-indicator value at the determined height should be maximized (or minimized), and the back-projected image points for the height should be tiepoints to each other, as indicated by the two search windows for P in Fig. 2. Because of this principle, OSBM methods can avoid quality degradation due to interpolation in DSM generation (Zhang et al., 2018). Additionally, they can easily impose various matching constraints, because all the tiepoints can be handled simultaneously in the matching process.

However, OSBM methods should predefine a height search range for vertical positioning. Therefore, these methods require an initial DSM to ensure high matching accuracy. Accordingly, the quality of the final results is inevitably dependent on the accuracy of the initial DSMs. For initial DSM generation, existing ISBM methods are effective. However, low-textured surfaces of sea-ice may cause ambiguity problems in image

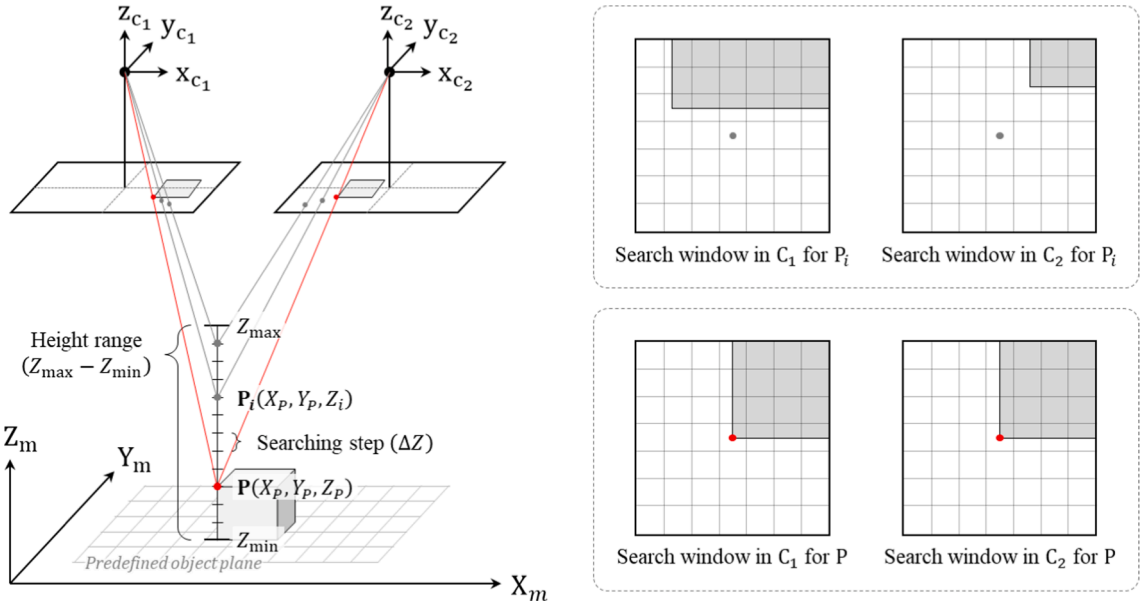

Fig. 2. Vertical positioning for each DSM grid in OSBM strategy.

matching, reducing the quality of DSMs. Therefore, to obtain improved results from incorrect initial DSMs, we derive a robust method for reliably determining the 3D positions of object points based on the optimized search-window sizes and matching constraints.

2.2. Relative georeferencing using terrestrial LiDAR

Georeferencing of sea-ice DSMs is difficult to achieve with structure-from-motion (SfM) photogrammetry methods, because sea ice is constantly drifting. To solve this problem, we use a terrestrial LiDAR dataset obtained for part of a target area. The sea-ice DSM derived from drone images is registered to the coordinate system of a LiDAR dataset. This approach focuses on recovering the horizontality and scale of the sea-ice DSM. Accordingly, we assume that the LiDAR datasets can contain the two properties. However, this requirement can be easily satisfied in practice, because terrestrial LiDAR systems can measure the distances to target objects while remaining level, and individual LiDAR datasets from different stations can be accurately merged using dedicated targets.

The proposed georeferencing method consists of approximation and optimization. In the first step, the transformation between the two datasets is approximately established from 3D tiepoints. Tiepoints are first extracted in 2D form from the drone mosaic and coloring point cloud, and then they are converted into 3D tiepoints using each DSM. The use of artificial targets such as checkerboards will make tiepoint extraction more reliable. In the second step, the approximated transformation is optimized, because the tiepoints extracted may include positional errors. For the optimization, we use the iterative closest point (ICP) algorithm (Besl and McKay, 1992; Chen and Medioni, 1992). The two-step transformation modeling can be formulated as follows:

$$\begin{bmatrix} X' \\ Y' \\ Z' \\ 1 \end{bmatrix} = \lambda \begin{bmatrix} r^o_{11} & r^o_{12} & r^o_{13} & t^o_x \\ r^o_{21} & r^o_{22} & r^o_{23} & t^o_y \\ r^o_{31} & r^o_{32} & r^o_{33} & t^o_z \\ 0 & 0 & 0 & 1 \end{bmatrix} \begin{bmatrix} r^a_{11} & r^a_{12} & r^a_{13} & t^a_x \\ r^a_{21} & r^a_{22} & r^a_{23} & t^a_y \\ r^a_{31} & r^a_{32} & r^a_{33} & t^a_z \\ 0 & 0 & 0 & 1 \end{bmatrix} \begin{bmatrix} X \\ Y \\ Z \\ 1 \end{bmatrix} \quad (1)$$

where (X, Y, Z) and (X', Y', Z') represent object points in target system and reference system, respectively; r^a and r^o represent the elements of rotation matrices for approximation and optimization, respectively; t^a and t^o represent the translation vectors for approximation and optimization, respectively; and λ represents the scale factor between the two coordinate systems.

The ICP algorithm estimates a transformation by selecting the pairs of object points that are closest to each other from two point clouds. This procedure is repeated until the transformation error reaches an acceptable level. Thus, there are two prerequisites for the ICP algorithm to work properly. First, the misalignment between the two datasets should be small. Second, reliable object points should be paired for accurate transformation estimation. The first requirement can be satisfied by the approximation step. However, the second one may not be satisfied, because initial DSMs created by the existing ISBM can contain considerable outliers. To dispel this concern, we use only reliable object points that are matched for three or more images in matching processes.

2.3. Determination of matching constraints

Match inspection aims to ensure the reliability of image matching on low-textured surfaces of sea ice by verifying matched points according to matching constraints. Match inspection regards as true matches only object points that satisfy all the constraints of matching indicators. Thus, to determine the matching constraints, measurements of matching indicators for true object points are required.

True object points are extracted from the LiDAR point cloud registered to the coordinate system of a drone dataset. After analysis-point extraction, matching indicators are measured with height errors using search windows of different sizes. The height error indicates the difference between the true height of an analysis point and the height estimated via vertical positioning. Measurements with large height errors are assumed to be results with inappropriate search windows and are therefore excluded from the matching constraints determination. Finally, constraints for each matching indicator are calculated from the mean and standard deviation of the valid measurements.

The location of a search window in each overlapping image is derived by a collinear equation. Among overlapping images, the image with the minimum relief displacement is defined as the reference image, to handle multiple drone images taken in unstable postures at low flight altitudes. The relief displacement is quantified as follows:

$$d = \left|\overrightarrow{PM}\right| + \left|\overrightarrow{PN}\right|, \quad (2)$$

where P, M, and N represent the target object point, the ground principal point, and the ground nadir point, respectively, as shown in Fig. 3.

The search window of a reference image is constructed with a larger area than the search windows of the remaining target images to measure the matching indicators. Accordingly, if the height of an object point is true, matches of target windows should be located at the center of a reference window.

As matching indicators, the ZNCC, matching distance error (MDE), matching point distribution (MPD), and modeling error (ME) are introduced (Kim et al., 2019b). The ZNCC is a representative matching indicator used in many applications. It is robust to radiometric differences (i.e. gain and constant offset) and noise (Hirschmuller and Scharstein, 2009). A ZNCC value closer to 1 indicates a stronger correlation.

The MDE and MPD are indicators of the accuracy and uncertainty, respectively, in image matching. Fig. 4 shows the concept of the two indicators. The MDE is defined as the mean of the error distances between matches of target windows (p_i) and the center of a reference window (c), as indicated by Eq. (3). The MPD is defined as the mean of error distances between matches of target windows and their center (c_p), as indicated by Eq. (4). Because the match of a target window is determined as the point with the maximum ZNCC value in a reference window, the MDE and MPD can be calculated in pixel units and should be zero for true object points. They can complement a limitation of the ZNCC: it is difficult to absolutely evaluate the validity of matches with the ZNCC. Thus, we use the MDE instead of the ZNCC as a key indicator for vertical positioning.

$$\text{MDE} = \frac{\sum_{i=1}^{N} \left|\overrightarrow{cp_i}\right|}{N}, \quad (3)$$

$$\text{MPD} = \frac{\sum_{i=1}^{N} \left|\overrightarrow{c_p p_i}\right|}{N}, \quad (4)$$

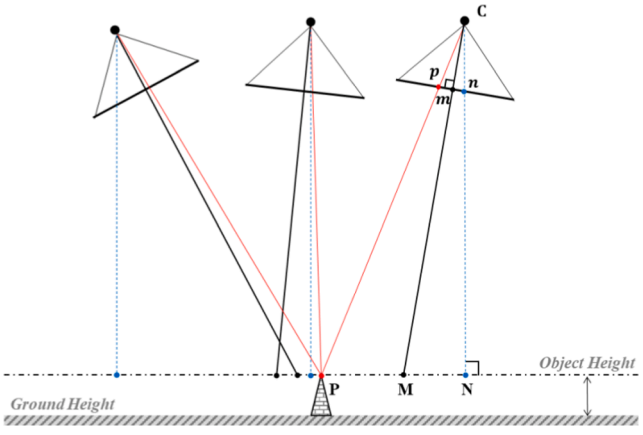

Fig. 3. Determination of a reference image to handle multiple drone images.

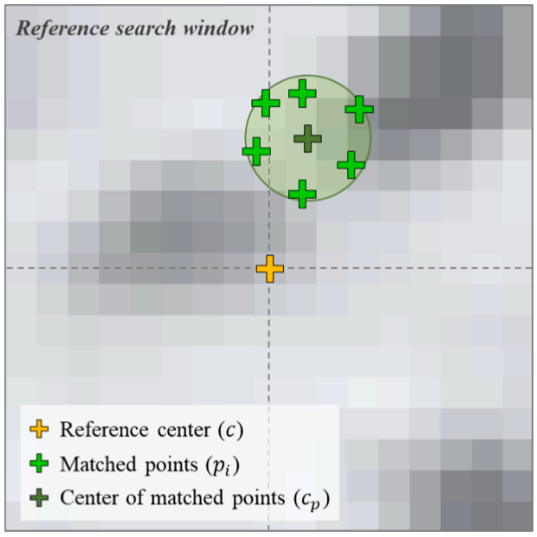

Fig. 4. Matched points of target windows on the reference window.

Here, N represents the number of target search windows.

The ME is also introduced to evaluate the matching uncertainty. In contrast to the other indicators, the ME represents the overall uncertainty in vertical positioning for a given object point. If the true height of an object point exists within a predefined height range, the matching-indicator values decrease as the height estimated via vertical positioning approaches the true height. However, the matching-indicator values fluctuate if the true height does not exist within the range, or if the matching uncertainty is large. Therefore, the ME is defined as the variation of the matching-indicator values, which is calculated using the differences between the measured and modeled matching-indicator values via Eq. (5). We use the MDE as a matching indicator for calculating the ME.

$$\mathrm{ME} = \sqrt{\frac{\sum_{i=1}^{M} (v_i^o - v_i^m)^2}{M}}, \tag{5}$$

Here, v_i^o and v_i^m represent the measured and modeled values of a matching indicator at the i^{th} height step, respectively, and M represents the number of height steps between $Z_{\min}$ and $Z_{\max}$.

Matching-indicator values may be asymmetric with respect to a true height and may also include spikes depending on the surface texture conditions. Therefore, we model the matching-indicator values using a third-order polynomial with the random sample consensus algorithm (Fischler and Bolles, 1981). The ME is used only for match inspection in robust vertical positioning.

2.4. Search-window size determination

The matching performance depends on not only the matching indicators but also on the search-window sizes. Thus, matching indicators should be calculated with sufficient textures for reliable image matching. Larger search windows contain more textures, but the search-window sizes should be restricted so that variations in elevation are not included (Veksler, 2003). Additionally, in image matching, the distinction of textures is more important than the amount of textures. Therefore, the optimal size of a search window should be defined as the smallest size with discernible texture information, and the window size should be adaptively adjusted according to the surface textures on the DSM grids. This consideration is particularly essential for sea ice, because the surface textures of sea ice are typically rare and can vary significantly among regions.

The proposed adaptive method derives and unifies optimal search-window candidates for each DSM grid. Optimal search-window candidates are derived via texture analysis. In texture analysis, reference search windows with different sizes are constructed, and their textures are quantified via entropy calculations using Eq. (6). Among the constructed search windows, optimal candidates are determined as search windows corresponding to peaks on the entropy curve, as shown in Fig. 5. This assumes that search windows with entropy peaks have distinct texture information from other search windows.

$$\mathrm{Entropy} = -\sum_k p_k \log_2(p_k), \tag{6}$$

Here, p_k represents the probability associated with gray level k.

The optimal window candidates are then unified via match inspection. Matching indicators are evaluated by applying the optimal window candidates in the order of size. During the match inspection, if a search window that satisfies the matching constraints is found, it is identified as a single optimal window for the DSM grid. Otherwise, all window candidates are considered in the subsequent vertical positioning.

Optimal search-window determination is conducted with an initial DSM. Accordingly, this process can also improve the quality of the initial DSM by removing values of DSM grids identified as mismatches and filling the holes. Therefore, repeating this process can increase the number of DSM grids with a single optimal window and improve the initial DSM.

2.5. Sea-ice surface reconstruction

In OSBM, the vertical position of the DSM grid is determined as the height with the maximum (or minimum) matching-indicator value. However, this approach is likely to cause mismatches on sea-ice surfaces, because the matching ambiguity caused by low-textured surfaces can increase the uncertainty in the matching-indicator values. Fig. 6 presents the MDE values measured along the vertical line on a grid of a sea-ice DSM. As shown, the height with the minimum value (yellow circle) may differ from the true height obtained from a LiDAR DSM, owing to the variations in the matching-indicator values. Therefore, to handle this uncertainty, we conduct vertical positioning using robustly modeled values instead of measurements (Kim et al., 2019b). As shown in Fig. 6, the MDE modeling consists of two steps: initial modeling and precision modeling. This two-step modeling aims to estimate the most probable height by reducing the height range for vertical positioning. The initial model is established from measurements for a full height range (blue line). The precision model is then established from measurements for a narrower height range around the minimum point of the initial model (red line).

After vertical positioning from the precision model, match inspection is performed. Therefore, a sea-ice DSM is constructed with only inlier

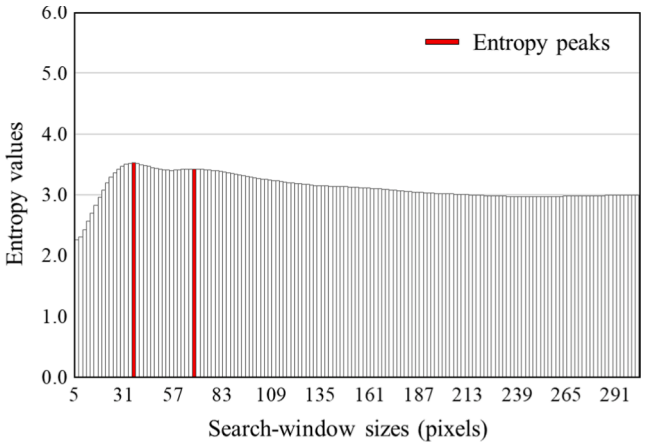

Fig. 5. Determination of optimal window candidates from entropy peaks.

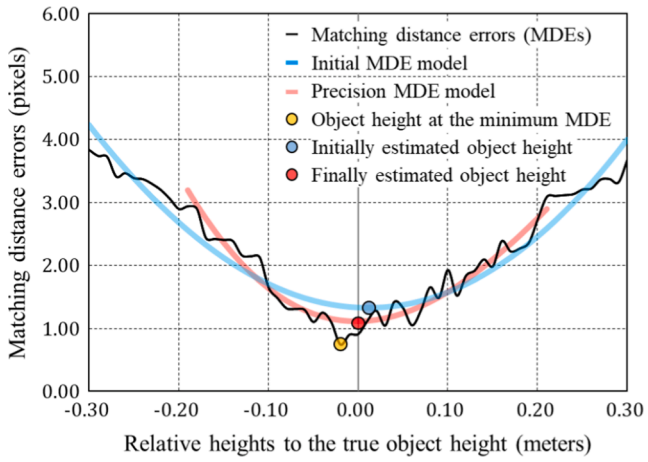

Fig. 6. Robust vertical positioning based on two-step MDE modeling.

grids. Holes in the sea-ice DSM are filled via inverse-distance-weighted interpolation from neighboring inlier grids. Finally, the sea-ice DSM is registered to the LiDAR DSM for georeferencing. To this end, the inverse of the transformation derived for selecting analysis points can be used.

2.6. Implementation and evaluation

The proposed method was implemented in the C++ language using OpenCV library (ver. 2.4.9) and GDAL library (ver. 2.0.2). The two libraries were mainly used for matrix computation and image handling. Experiments were conducted on a 64-bit Windows 10 platform with an Intel Core i9-9900 K central processing unit (clock speed of 3.6 GHz, 64 GB of random-access memory).

The performance of the proposed method was evaluated according to the height errors between the generated sea-ice DSM and the observed LiDAR point cloud. From the height errors, we calculated the mean error, RMS error (RMSE), standard deviation (SD), median, linear error (LE), and normalized median absolute deviation (NMAD). In contrast to the first three measures, the median, LE, and NMAD are effective if normality of the error distribution cannot be assumed due to outliers (Höhle and Höhle, 2009). The median indicates the 50th percentile. The

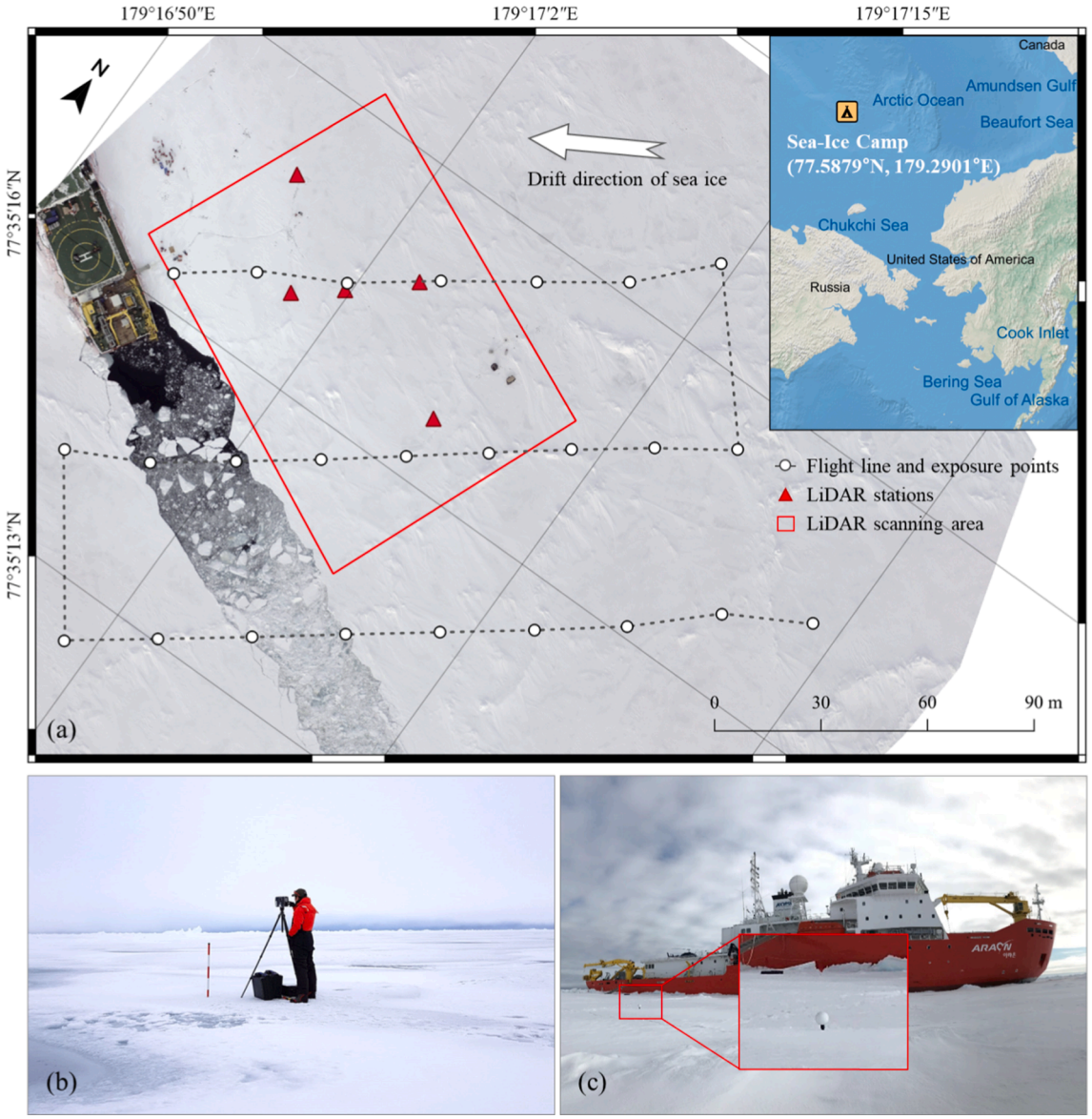

Fig. 7. Overview of the dataset acquisition on the drifting sea ice: (a) Study site and data-acquisition plan; (b) Terrestrial LiDAR scanning; (c) Deployed sphere target.

LE represents the absolute vertical accuracy at a specific confidence level. For example, the LE at 95% confidence (LE95) means that a minimum of 95% of DSM grids has a height error less than the determined LE95 value. The NMAD can be considered as a robust estimate for the SD.

3. Results and discussion

3.1. Study site and datasets

Datasets for DSM generation were obtained during an Arctic sea-ice campaign in August 2017 using the Korea Icebreaker Research Vessel (IBRV) Araon. The Araon vessel was anchored to drifting sea ice for 2 d. Fig. 7 shows the location of the sea-ice camp and an overview of data acquisition on the drifting sea ice.

For aerial image acquisition, a lightweight drone (DJI Phantom 4, DJI, Shenzhen, China) with a total weight of 1.4 kg and a maximum flight time of 28 min was used. The camera sensor mounted on the drone was an FC330, with an image size of 4000 × 3000 pixels, a focal length of 3.6 mm, and a pixel size of 1.58 μm. We collected 25 images by manually controlling the drone at an altitude of 50 m and a velocity of 3 m/s. Due to the drift of sea ice, automated drone flight and geotagging of images based on real-time kinematic (RTK) or post-processed kinematic (PPK) could not be considered. On the other hand, we tried to obtain images with high overlaps in the flight route of a regular grid pattern. Accordingly, 77% frontal overlap and 55% side overlap were established between the acquired images.

The Araon vessel was equipped with various observation sensors, such as GNSS/INS, temperature, and wind sensors. According to the measurements during the image acquisition time of 3 min and 33 s, the sea ice moved linearly at a velocity of 0.16 m/s, and the average air temperature and wind speed were −0.86 °C and 13.3 m/s, respectively.

The drone images were processed by the commercial software Pix4D 4.1.24 (Pix4D SA, Lausanne, Switzerland). The interior and exterior camera parameters were estimated without GCPs. The mean reprojection error in the bundle adjustment was approximately 0.2 pixels for the 40,563 matched object points. In general, the GNSS/INS data tagged in images should be corrected to the drift of sea ice before estimating the camera parameters. However, in our case, there was no significant difference in the results before and after the correction, because the drift of the sea ice was not large during the image acquisition. Mosaic and DSM were produced through dense image matching. The spatial-resolution and total area of the products were 4 cm and 0.062 km^2, respectively. Fig. 8 presents the resulting mosaic and DSM.

For LiDAR data acquisition, a terrestrial laser scanner (Focus3D X130, FARO, Lake Mary, FL, USA) with a distance range of 0.6–130 m, a precision of 2 mm, a vertical rotation range of 300°, and a horizontal rotation range of 360° was used. This laser scanner provides colored point clouds. We collected point clouds from five stations near the Araon vessel for 2 h 15 min, as shown in Fig. 7(a) and (b). Since the sea ice was large enough not to be affected by wind and tide, the scanner could be precisely leveled at each station. The attitude variations of the sea ice, measured during the acquisition time, were approximately 0.005° and 0.003° for the roll and pitch angles, respectively.

LiDAR point clouds were processed by the software FARO SCENE 6.2.4.30. Using sphere targets deployed on the sea ice (Fig. 7(c)), the point clouds were accurately registered and merged. The horizontal and vertical errors were 2.4 mm and 1.2 mm, respectively. The coloring point cloud and DSM were produced with a spatial-resolution of 1 cm from the merged point cloud. Fig. 9 shows the resulting coloring point cloud and DSM defined in a local coordinate system. Holes in the two products were filled by interpolating neighbor pixels for efficient registration between the LiDAR dataset and the drone dataset.

3.2. Results of sea-ice DSM generation

Registration of the LiDAR dataset to the drone dataset preceded the determination of the matching constraints. Because of the low-textured surfaces of the sea ice, we selected tiepoints mainly from footprints in the snow and blocks of ice, as shown in Fig. 10(a) and (c). Unfortunately, we did not deploy checkerboards at the time of the data acquisition. After two-step transformation modeling, the LiDAR point cloud (instead of the LiDAR DSM) was registered. This was intended to avoid selecting analysis points from filled holes in the LiDAR DSM. The horizontal and vertical errors of the registration were 2.7 cm and 2.6 cm, respectively. This registration accuracy was considered acceptable in that the ground sampling distance (GSD) of the drone images was 4 cm.

To avoid subjective intervention in selecting surface textures for

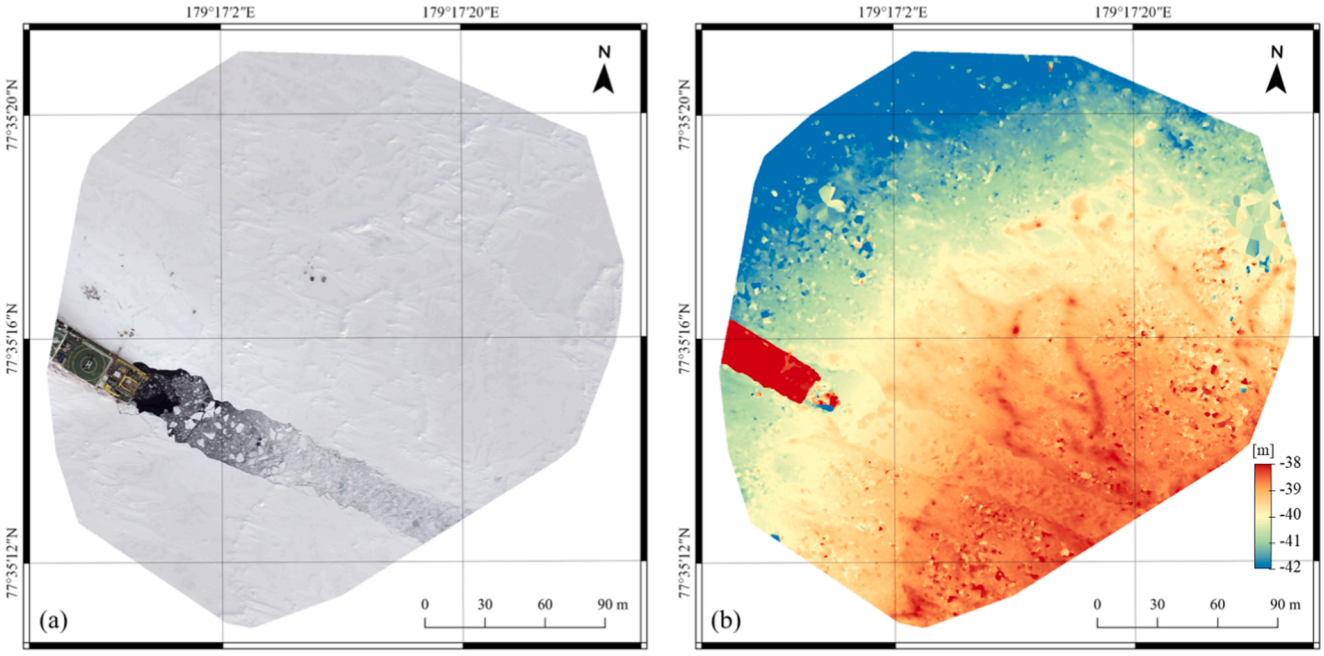

Fig. 8. Drone image processing results: (a) Mosaic; (b) DSM.

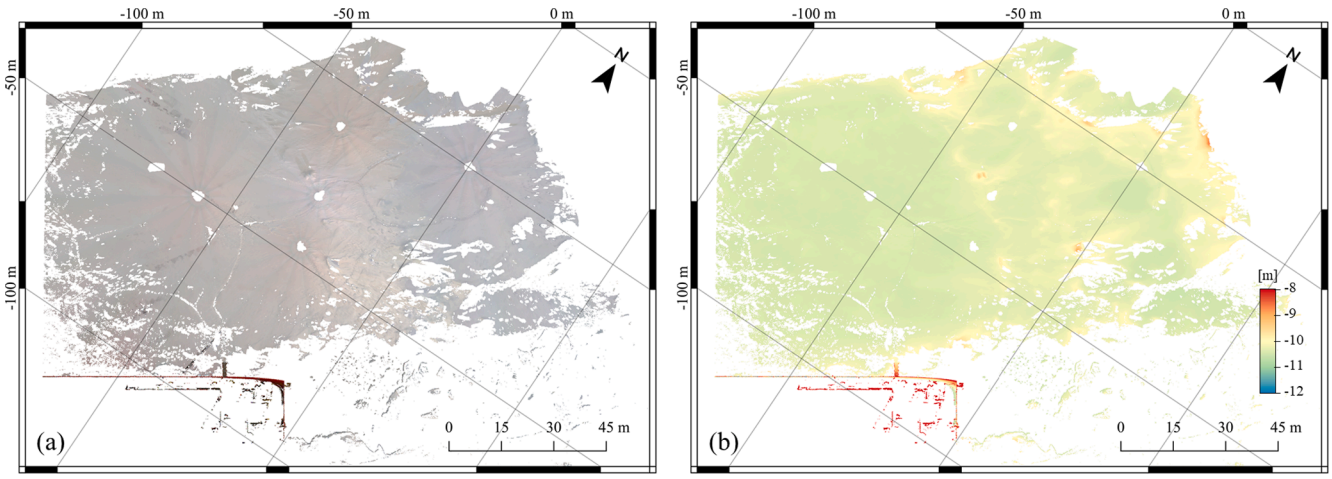

Fig. 9. LiDAR data-processing results: (a) Coloring point cloud; (b) DSM. This figure was formulated by editing Fig. 5 from the work of Kim et al. (2019b).

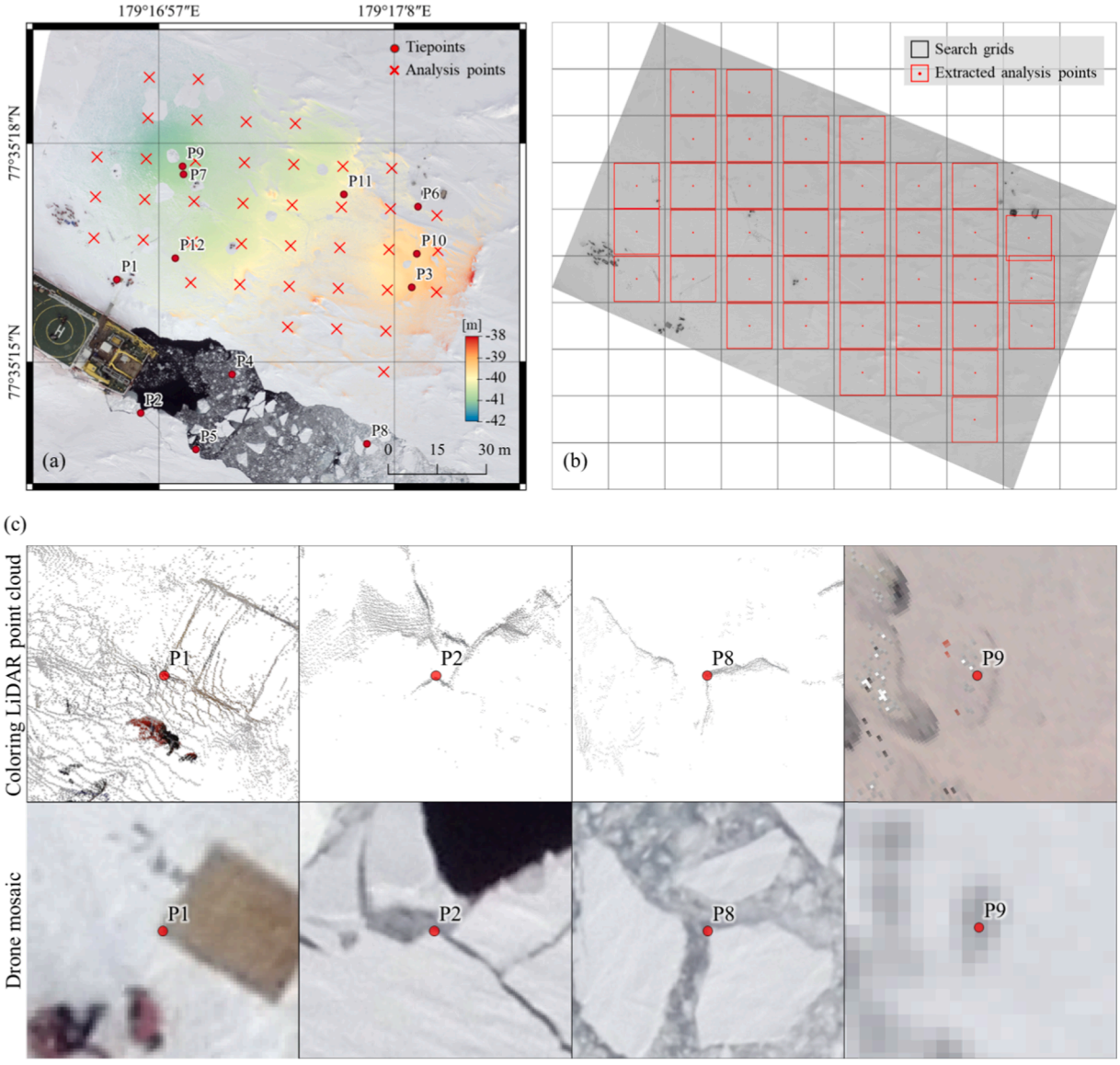

Fig. 10. Registration of the LiDAR point cloud and extraction of analysis points: (a) LiDAR point cloud registered and tiepoints used; (b) Analysis points extracted in search grids; (c) Locations of the extracted tiepoints. This figure was formulated by editing Fig. 5 from the work of Kim et al. (2019b).

matching-indicator analysis, we partitioned the LiDAR scanning area into search grids with the same size and selected the points closest to the center of each grid as analysis points (Fig. 10(b)). Accordingly, 39 analysis points were automatically extracted, and the matching indicators were measured at these points. Different search-window sizes ranging from 7 × 7 to 301 × 301 pixels with 2-pixel intervals were applied. Measurements with height errors larger than twice the GSD of the drone images were excluded from the matching-indicator analysis. Fig. 11 shows the scatterplots between measurements of matching indicators and height errors. These scatterplots show that the matching indicators were closely related to the matching errors and that the MDE better reflected the matching errors than the ZNCC, which has traditionally been used.

Constraints of the matching indicators were finally determined in the 95% confidence interval for the accepted measurements (i.e. mean ± 2 sigma). Table 1 presents the statistics and constraints for each matching indicator. Considering the allowed value ranges for the matching indicators, the minimum and maximum values of the constraints were adjusted.

After determination of the matching constraints, a sea-ice DSM was generated through optimal search-window determination and sea-ice surface reconstruction. Fig. 12 shows the intermediate and final results for the LiDAR scanning area of 0.0091 km^2. As an initial DSM for vertical positioning, the drone DSM, which was produced by the commercial software, was used (Fig. 8(b)). Predictably, the initial DSM contained many matching errors compared with the LiDAR point cloud, which were distributed mainly on low-textured surfaces (Fig. 12(a) and (b)). Additionally, the initial DSM appeared to be horizontally tilted. This may be because the established object-space coordinate system did not correctly reflect the real world, owing to the exterior orientation without GCPs.

Table 1
Constraints of matching indicators determined from the accepted measurements.

	Statistics		Constraints	
Indicators	Mean	SD	Minimum	Maximum
MDE (pixels)	0.98	0.51	0.00	2.00
MPD (pixels)	0.63	0.39	0.00	1.41
ZNCC	0.65	0.16	0.32	1.00
ME (pixels)	0.21	0.17	0.00	0.56

The optimal search-window sizes were determined through surface-texture analysis. Optimal window-size candidates for each DSM grid were derived from entropy peaks and unified via match inspection. During this process, mismatches in the initial DSM were detected and removed (Fig. 12(c)), and the remaining holes were filled from neighboring inlier pixels (Fig. 12(d)). A comparison between Fig. 12(b) and (c) indicates that the detection results responded well to perceptible matching errors in the initial DSM. To quantitatively evaluate the detection results, we calculated the confusion matrix and several performance indicators using the registered LiDAR point cloud, as shown in Table 2. Grids of the initial DSM with height errors larger than twice the GSD were regarded as mismatches. The recall (sensitivity), i.e., the ratio of the number of correctly detected true matches to the total number of true matches, was approximately 92%. However, the precision, i.e., the ratio of the number of correctly detected true matches to the number of detected true matches, was relatively low (approximately 74%). In addition, the accuracy, which is the ratio of the number of correctly detected matches to the total number of matches, was similar to the precision. Thus, numerous mismatches were classified as inliers. These results may not satisfy the required performance for an error detector.

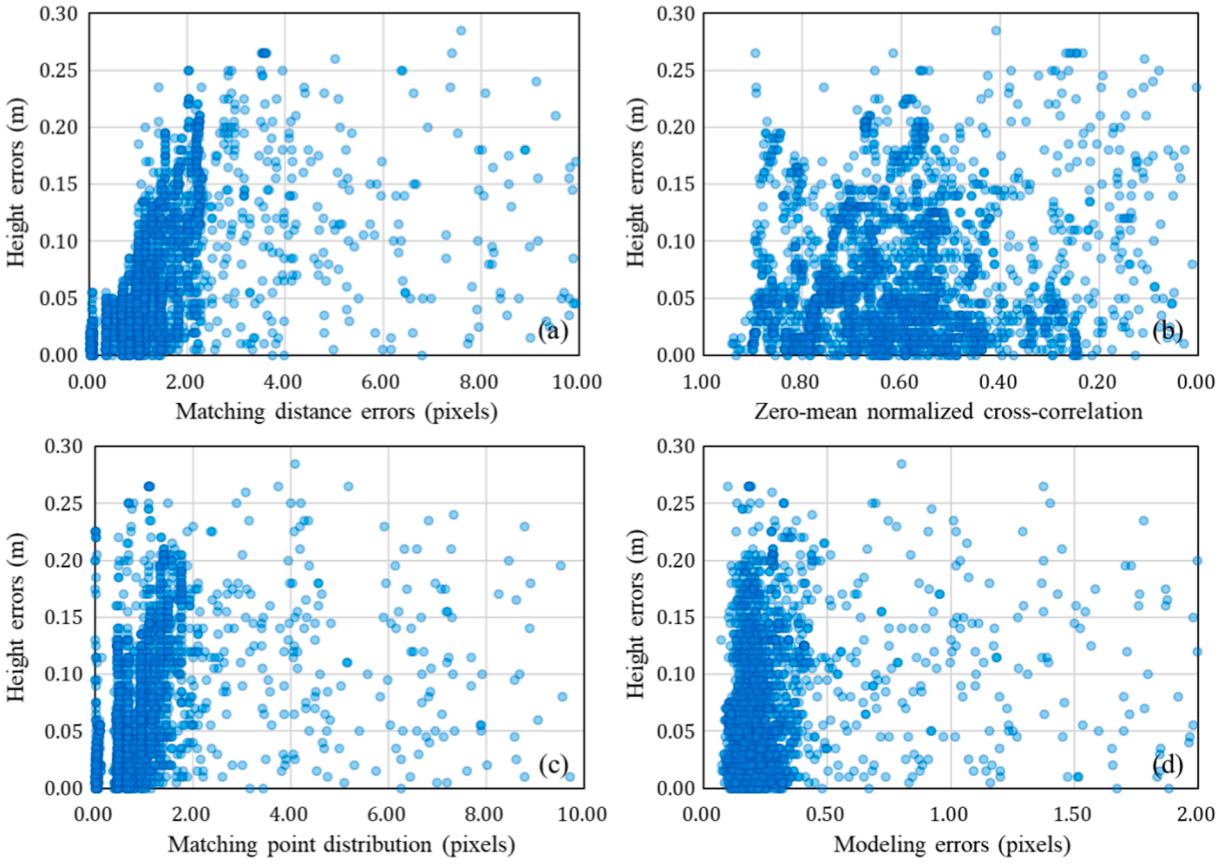

Fig. 11. Scatterplots between measurements of matching indicators and errors of vertical positioning for different search-window sizes: (a) MDE; (b) ZNCC; (c) MPD; (d) ME.

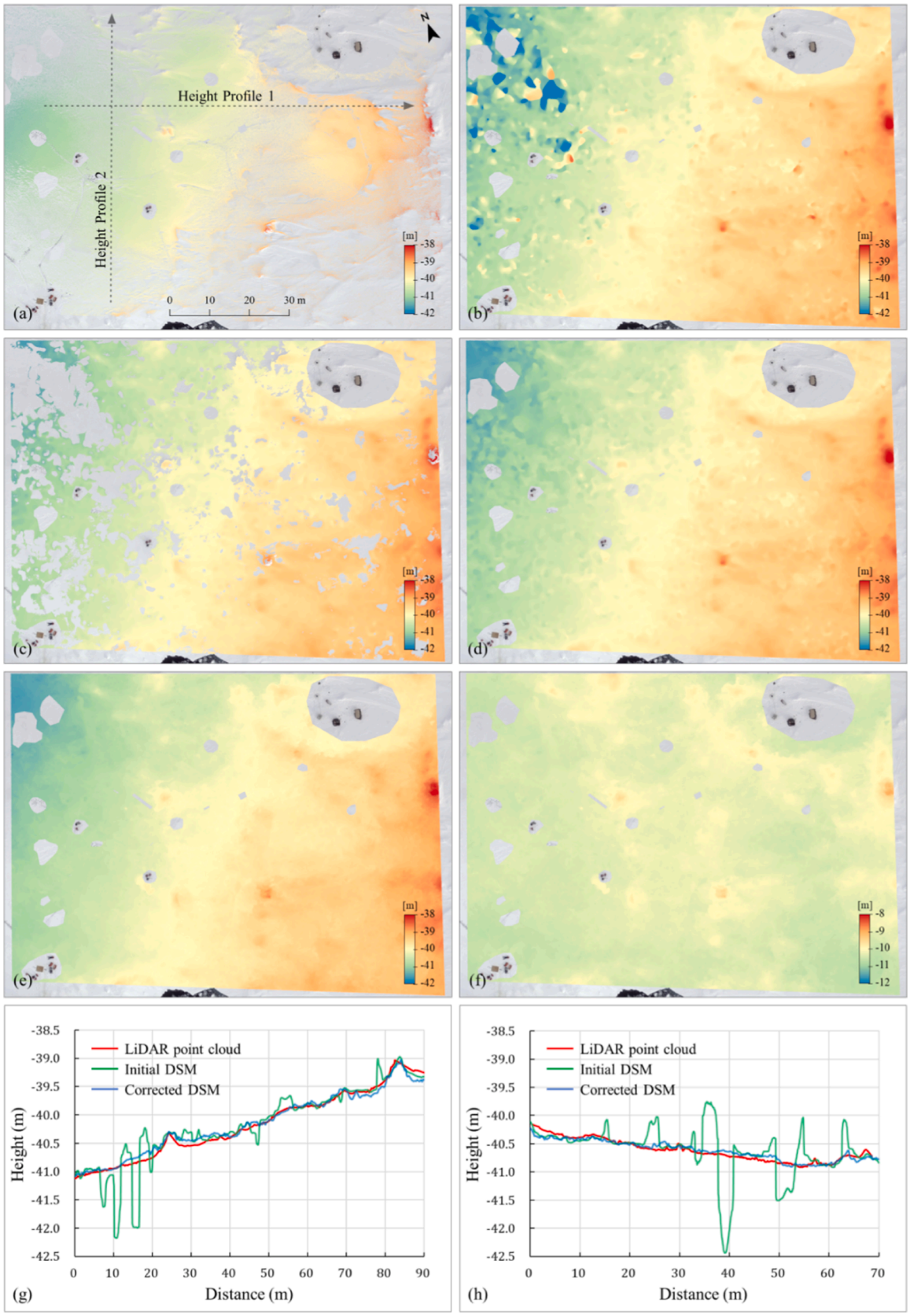

Fig. 12. Sea-ice DSMs generated for the LiDAR scanning area: (a) LiDAR point cloud; (b) Initial DSM; (c) Initial DSM filtered for mismatches; (d) Enhanced initial DSM; (e) Corrected DSM; (f) Georeferenced final DSM; (g) Height profile 1; (h) Height profile 2.

Table 2
Confusion matrix and performance indicators for the mismatch detection results.

N = 1832878	Detected: Yes	Detected: No	Recall	0.92
Actual: Yes	1,084,923	88,819	Precision	0.74
Actual: No	386,092	273,044	Accuracy	0.74

However, they are acceptable in our case, because the hole-filled result is only used as an initial DSM for vertical positioning.

The sea-ice DSM was generated through robust vertical positioning from the derived optimal windows and the enhanced initial DSM. Since the proposed method involves the match inspection to verify the matched points, we did not carry out an additional process to deal with outliers. Compared with the initial DSM in Fig. 12(b), the quality improvement of the resulting DSM was remarkable. Even compared with the enhanced initial DSM in Fig. 12(c), we identified noticeable improvements, such as smooth transitions in elevation. Detailed comparisons are presented in Fig. 12(g) and (h). The corrected DSM well reflected the height changes of the LiDAR point cloud and also produced reliable matching results even for low-textured surfaces. This was also confirmed in the quantitative evaluation, as indicated by Table 3. We calculated height error statistics using all the object-point pairs between the sea-ice DSM and the registered LiDAR point cloud, as in the evaluation of the mismatch detection results. For both the initial DSM and the corrected DSM, the mean errors were close to zero, and the differences between the mean and median errors were also small. Although the corrected DSM showed slightly better results, the differences were not significant. These results indicate that both the DSMs were not systematically shifted and that the registration for relative georeferencing was accurately established. On the other hand, the RMSEs revealed considerable differences. The RMSE, which was approximately 26 cm in the initial DSM, decreased to approximately 8 cm in the corrected DSM. Both the minimum and maximum height errors were significantly reduced. Furthermore, the SD and NMAD were approximately the same, and the LE95 converged to 1.96 times the SD. These results indicate that the height errors of the corrected DSM follow a normal distribution without outliers.

The sea-ice DSM was finally registered to the LiDAR dataset for georeferencing. Accordingly, the tilted sea-ice DSM was restored correctly to sea level, as shown in Fig. 12(f). The georeferenced sea-ice DSM consisted of negative heights, because the heights of the LiDAR point cloud were measured by a barometric height sensor embedded in the laser scanner. Therefore, to obtain the freeboard of the sea ice, the resulting DSM should be translated vertically to sea level. The sea-level height can be measured from open water exposed by the icebreaker. The sea-ice DSMs for the whole imaging area are shown in Fig. 13. These results also indicated high-quality matching without significant errors. From the derived freeboard of the sea ice, the mean and maximum thicknesses were 1.02 m and 3.04 m, respectively. The roughness of the sea ice, defined as the standard deviation of elevations, was 32 cm. These measurements suggest that the study site was probably first-year sea-ice (Han et al., 2020).

The total processing time was approximately 41.56 h. This indicates that the proposed method is time-consuming compared to the processing time of Pix4D, which took approximately 0.44 h. However, the proposed method would still be valuable for applications that need to prioritize the quality of DSMs. Moreover, there is still room for improvement, such as graphics processing unit (GPU)-based parallel processing.

3.3. Performance analysis

To create DSMs of drifting sea ice with low-textured surfaces, the proposed method introduced four new considerations: relative georeferencing, match inspection, optimal window selection, and robust vertical positioning. Accordingly, the proposed method produced a significantly improved DSM compared with the initial DSM. The height error statistics quantitatively demonstrated the improvement.

The performance of the individual considerations was evaluated using the 39 analysis points (Fig. 10(a)). In this analysis, relative georeferencing was excluded, because it is not directly related to the performance of image matching. Table 4 presents the results of the performance evaluation. Here, the height errors corresponding to the mean represent RMSEs, in contrast to the results for the search-window sizes.

We first analyzed the performance of match inspection by applying different combinations of the matching indicators. The height errors gradually decreased as additional matching indicators were used (top to bottom in Table 4). These results indicate that all the matching indicators contributed to the validation of the matches. Thus, the match inspection can improve not only the initial DSM, as shown in Fig. 12(d), but also the results of vertical positioning. Thus far, matching methods have used only a single matching indicator (Banks and Corke, 2001; Hirschmuller and Scharstein, 2009). However, the comparison results suggest that various matching indicators should be considered for reducing the matching uncertainty, particularly in generating sea-ice DSMs.

The optimal window selection was analyzed through comparison with a simple adaptive method (Zhang et al., 2010). This simple adaptive method identified the optimal window size by sequentially applying all the window sizes from the smallest to the largest. Accordingly, the optimal window sizes derived by the simple adaptive method were smaller than those derived by the proposed method. However, the height errors were significantly larger. These results indicate that although the optimal window sizes can be minimized by considering all the window sizes, windows with matching ambiguity may also be selected as optimal windows. The proposed method, which can derive optimal window candidates or unify them, exhibited better results. The comparison revealed that our method can more clearly determine search windows with distinct texture information, improving both its efficiency and accuracy in image matching.

Lastly, robust vertical positioning was analyzed via comparison with the existing method of determining the height of a DSM grid using the minimum matching-indicator value (Zhang et al., 2017, 2018). The existing method yielded larger height errors. The degradation was most severe when all window sizes were considered (the first case in Table 4). This was probably due to the negative effects of search windows with matching ambiguity on the measurement of the matching indicators. The results of the second case using our window selection method support this argument. Additionally, the fourth case exhibited better results than the second case. Overall, these findings indicate that the proposed vertical positioning method correctly handled the matching uncertainty for low-textured surfaces. According to the evaluation results, among our considerations, the robust vertical positioning method made the most significant contribution to the quality enhancement.

4. Conclusions

Arctic sea-ice DSMs can be effectively used not only for developing

Table 3
Height error statistics of sea-ice DSMs for the LiDAR scanning area (unit: meters).

DSMs	Minimum	Maximum	Mean	SD	RMSE	Median	NMAD	LE95
Initial	–3.9697	2.1306	0.0167	0.2612	0.2618	0.0228	0.0790	0.3341
Corrected	–0.7990	0.5586	0.0127	0.0828	0.0838	0.0143	0.0743	0.1610

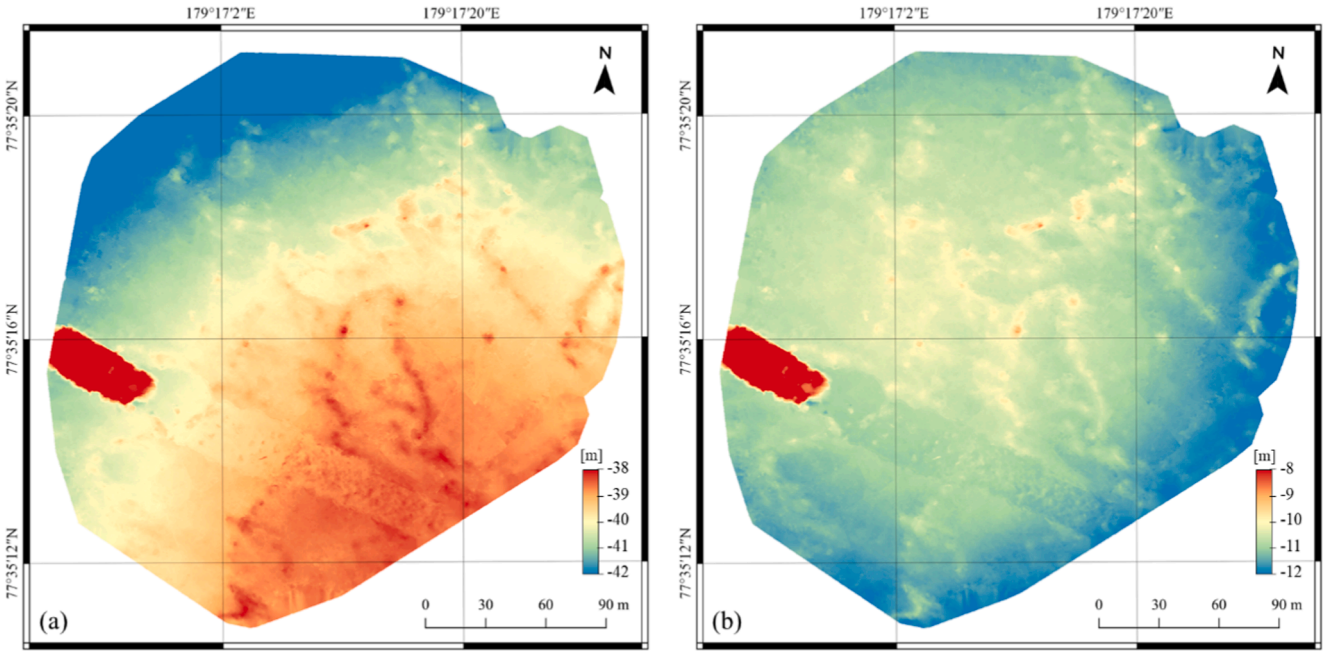

Fig. 13. Sea-ice DSMs generated for the whole drone-imaging area: (a) Corrected DSM for the whole imaging area; (b) Georeferenced DSM for the whole imaging area.

Table 4
Search-window sizes (w) and height errors (h) derived by different matching methods (unit: pixels for search-window sizes and meters for height errors). Height errors corresponding to the mean represent RMSEs.

Vertical positioning		MDE measuring				MDE modeling			
Window selection		All windows		Texture analysis		All windows		Texture analysis	
Match inspection		w	$\|h\|$	w	$\|h\|$	w	$\|h\|$	w	$\|h\|$
MDE	Mean	31	0.1116	50	0.0838	32	0.0772	52	0.0650
	SD	21		35		21		33	
	Minimum	7	0.0000	7	0.0000	7	0.0000	15	0.0050
	Maximum	101	0.2600	135	0.1800	101	0.1950	135	0.1350
MDE and MPV	Mean	34	0.1084	52	0.0829	34	0.0701	53	0.0637
	SD	21		34		21		33	
	Minimum	7	0.0000	13	0.0000	7	0.0000	15	0.0050
	Maximum	101	0.2600	135	0.1800	101	0.1700	135	0.1350
MDE, MPV, and ZNCC	Mean	38	0.1063	61	0.0762	38	0.0692	61	0.0637
	SD	26		38		26		38	
	Minimum	7	0.0000	15	0.0000	7	0.0000	15	0.0050
	Maximum	111	0.2600	153	0.1800	111	0.1700	153	0.1350
All indicators	Mean	–	–	–	–	41	0.0696	70	0.0607
	SD	–	–	–	–	26		43	
	Minimum	–	–	–	–	9	0.0000	15	0.0050
	Maximum	–	–	–	–	111	0.1250	183	0.1350

satellite-based remote-sensing methods as ground truth but also for precisely analyzing sea-ice topography. This paper proposes a robust DSM generation method for drifting sea ice. To overcome the problems in georeferencing and image matching, caused by the movement and low-textured surfaces of sea ice, the proposed method includes four improvements: relative georeferencing to recover the horizontality and scale of sea-ice DSMs, match inspection to verify the matched points, adaptive search-window adjustment to ensure distinct texture information, and robust vertical positioning to reduce the matching uncertainty. Experimental results indicated that the proposed method can achieve significant quality improvements (the RMSE of approximately 8 cm) compared with the existing ISBM method (the RMSE of approximately 26 cm) and that all our considerations contributed significantly to the improvements.

Although this paper proposes effective considerations for generating Arctic sea-ice DSMs, the basic matching strategy of the proposed method is based on that of the traditional method. This suggests that the proposed method can be improved with regard to efficiency and reliability by applying recent advances in image-matching techniques. Additionally, we will utilize the proposed method for various cryosphere studies. As our method is capable of generating high-quality sea-ice DSMs, we will first analyze the effects of topographical characteristics on changes in the sea ice, such as the creation and development of melt ponds. We also expect that the proposed method can be used not only in other cryosphere regions such as glaciers, ice sheets, and ice shelves but also in other special regions such as deserts.

Declaration of Competing Interest

The authors declare that they have no known competing financial

interests or personal relationships that could have appeared to influence the work reported in this paper.

Acknowledgments

This research was funded by the Korea Polar Research Institute (KOPRI), Grant PE20080 (Study on remote sensing for quantitative analysis of changes in the Arctic cryosphere).

References

Banks, J., Corke, P., 2001. Quantitative evaluation of matching methods and validity measures for stereo vision. Int. J. Robot. Res. 20 (7), 512–532. https://doi.org/10.1177/02783640122067525.

Besl, P.J., McKay, N.D., 1992. A method for registration of 3-D shapes. IEEE Trans. Pattern Anal. Mach. Intell. 14 (2), 239–256. https://doi.org/10.1109/34.121791.

Chen, Y., Medioni, G., 1992. Object modelling by registration of multiple range images. Image Vision Comput. 10 (3), 145–155. https://doi.org/10.1016/0262-8856(92)90066-C.

Chiang, K.-W., Tsai, M.-L., Chu, C.-H., 2012. The development of an UAV borne direct georeferenced photogrammetric platform for ground control point free applications. Sensors 12 (7), 9161–9180. https://doi.org/10.3390/s120709161.

Clapuyt, F., Vanacker, V., Van Oost, K., 2016. Reproducibility of UAV-based earth topography reconstructions based on Structure-from-Motion algorithms. Geomorphology 260, 4–15. https://doi.org/10.1016/j.geomorph.2015.05.011.

Divine, D.V., Pedersen, C.A., Karlsen, T.I., Aas, H.F., Granskog, M.A., Hudson, S.R., Gerland, S., 2016. Photogrammetric retrieval and analysis of small scale sea ice topography during summer melt. Cold Reg. Sci. Technol. 129, 77–84. https://doi.org/10.1016/j.coldregions.2016.06.006.

Eicken, H., Grenfell, T.C., Perovich, D.K., Richter-Menge, J.A., Frey, K., 2004. Hydraulic controls of summer Arctic pack ice albedo. J. Geophys. Res. 109 (C8), 1–12. https://doi.org/10.1029/2003JC001989.

Elboher, E., Werman, M., 2013. Asymmetric correlation: a noise robust similarity measure for template matching. IEEE Trans. Image Process. 22, 3062–3073. https://doi.org/10.1109/TIP.2013.2257811.

Fischler, M.A., Bolles, R.C., 1981. Random sample consensus: a paradigm for model fitting with applications to image analysis and automated cartography. Commun. ACM 24, 381–395. https://doi.org/10.1145/358669.358692.

Fusiello, A., Roberto, V., Trucco, E., 1997. Efficient stereo with multiple windowing. In: Proc. IEEE Computer Society Conference on Computer Vision and Pattern Recognition, San Juan, USA, 17–19 June. pp. 858–863. doi: 10.1109/CVPR.1997.609428.

Gonçalves, J.A., Henriques, R., 2015. UAV photogrammetry for topographic monitoring of coastal areas. ISPRS J. Photogramm. Remote Sens. 104, 101–111. https://doi.org/10.1016/j.isprsjprs.2015.02.009.

Hagen, R.A., Peters, M.F., Liang, R.T., Ball, D.G., Brozena, J.M., 2014. Measuring Arctic sea ice motion in real time with photogrammetry. IEEE Geosci. Remote S. 11 (11), 1956–1960. https://doi.org/10.1109/LGRS.2014.2314958.

Han, H., Kim, J.-I., Hyun, C.-U., Kim, S.H., Park, J.-W., Kwon, Y.-J., Kim, H.-C., 2020. Surface roughness signatures of summer arctic snow-covered sea ice in X-band dual-polarimetric SAR. GISci. Remote Sens. 57 (5), 650–669. https://doi.org/10.1080/15481603.2020.1767857.

Hendricks, S., Stenseng, L., Helm, V., Haas, C., 2010. Effects of surface roughness on sea ice freeboard retrieval with an Airborne Ku-Band SAR radar altimeter. In: Proc. IEEE International Geoscience and Remote Sensing Symposium, Honolulu, USA, 25–30 July, pp. 3126–3129. https://doi.org/10.1109/IGARSS.2010.5654350.

Helgesen, H.H., Leira, F.S., Bryne, T.H., Albrektsen, S.M., Johansen, T.A., 2019. Real-time georeferencing of thermal images using small fixed-wing UAVs in maritime environments. ISPRS J. Photogramm. Remote Sens. 154, 84–97. https://doi.org/10.1016/j.isprsjprs.2019.05.009.

Hirschmüller, H., Innocent, P.R., Garibaldi, J., 2002. Real-time correlation-based stereo vision with reduced border errors. Int. J. Comput. Vis. 47, 229–246. https://doi.org/10.1023/A:1014554110407.

Hirschmuller, H., Scharstein, D., 2007. Evaluation of cost functions for stereo matching. In: Proc. IEEE Conference on Computer Vision and Pattern Recognition, Minneapolis, USA, 17-22 June. pp. 1–8. doi: 10.1109/CVPR.2007.383248.

Hirschmuller, H., Scharstein, D., 2009. Evaluation of stereo matching costs on images with radiometric differences. IEEE Trans. Pattern Anal. Mach. Intell. 31 (9), 1582–1599. https://doi.org/10.1109/TPAMI.2008.221.

Höhle, J., Höhle, M., 2009. Accuracy assessment of digital elevation models by means of robust statistical methods. ISPRS J. Photogramm. Remote Sens. 64 (4), 398–406. https://doi.org/10.1016/j.isprsjprs.2009.02.003.

Hong, S.-H., Wdowinski, S., Amelung, F., Kim, H.-C., Won, J.-S., Kim, S.-W., 2018. Using TanDEM-X pursuit monostatic observations with a large perpendicular baseline to extract glacial topography. Remote Sens. 10 (11), 1851. https://doi.org/10.3390/rs10111851.

Kanade, T., Okutomi, M., 1994. A stereo matching algorithm with an adaptive window: theory and experiment. IEEE Trans. Pattern Anal. Mach. Intell. 16 (9), 920–932. https://doi.org/10.1109/34.310690.

Kang, S.B., Szeliski, R., Chai, J., 2001. Handling occlusions in dense multi-view stereo. In: Proc. IEEE Computer Society Conference on Computer Vision and Pattern Recognition, Kauai, USA, 8–14 December. pp. I-103-I-110. doi: 10.1109/CVPR.2001.990462.

Karvonen, J., Cheng, B., Vihma, T., Arkett, M., Carrieres, T., 2012. A method for sea-ice thickness and concentration analysis based on SAR data and a thermodynamic model. Cryosphere 6, 1507–1526. https://doi.org/10.5194/tc-6-1507-2012.

Kim, H., Han, H., Hyun, C., Chi, J., Son, Y., Lee, S., 2019a. Research on analytical technique for satellite observation of the Arctic sea ice. Korea J. Remote Sens. 34 (6_2), 1283–1298. https://doi.org/10.7780/kjrs.2018.34.6.2.12.

Kim, J.-I., Kim, H.-C., 2018. Incorrect match detection method for Arctic sea-ice reconstruction using UAV images. Int. Arch. Photogramm. Remote Sens. Spatial Inf. Sci. XLII-2, 501–505. doi: 10.5194/isprs-archives-XLII-2-501-2018.

Kim, J.-I., Hyun, C.-U., Han, H., Kim, H., 2019b. Evaluation of matching costs for high-quality sea-ice surface reconstruction from aerial images. Remote Sens. 11 (9), 1055. https://doi.org/10.3390/rs11091055.

Lang, A., Yang, S., Kaas, E., 2017. Sea ice thickness and recent Arctic warming. Geophys. Res. Lett. 44 (1), 409–418. https://doi.org/10.1002/2016GL071274.

Meier, W.N., Hovelsrud, G.K., van Oort, B.E.H., Key, J.R., Kovacs, K.M., Michel, C., Reist, J.D., 2014. Arctic sea ice in transformation: a review of recent observed changes and impacts on biology and human activity. Rev. Geophys. 52 (3), 185–217. https://doi.org/10.1002/2013RG000431.

Nolin, A.W., Mar, E., 2019. Arctic sea ice surface roughness estimated from multi-angular reflectance satellite imagery. Remote Sens. 11 (1), 50. https://doi.org/10.3390/rs11010050.

Padró, J.-C., Muñoz, F.-J., Planas, J., Pons, X., 2019. Comparison of four UAV georeferencing methods for environmental monitoring purposes focusing on the combined use with airborne and satellite remote sensing platforms. Int. J. Appl. Earth Obs. 75, 130–140. https://doi.org/10.1016/j.jag.2018.10.018.

Pistone, K., Eisenman, I., Ramanathan, V., 2014. Observational determination of albedo decrease caused by vanishing Arctic sea ice. Proc. Natl. Acad. Sci. 111 (9), 3322–3326. https://doi.org/10.1073/pnas.1318201111.

Pluim, J.P.W., Maintz, J.B.A., Viergever, M.A., 2003. Mutual-information-based registration of medical images: a survey. IEEE Trans. Med. Imaging 22 (8), 986–1004. https://doi.org/10.1109/TMI.2003.815867.

Scharien, R.K., Yackel, J.J., 2005. Analysis of surface roughness and morphology of first-year sea ice melt ponds: implications for microwave backscatter. IEEE Trans. Geosci. Remote Sens. 43 (12), 2927–2939. https://doi.org/10.1109/TGRS.2005.857896.

Shi, H., Zhu, H., Wang, J., Yu, S.-Y., Fu, Z.-F., 2016. Segment-based adaptive window and multi-feature fusion for stereo matching. J. Algorithms Comput. Technol. 10 (1), 3–11. doi: 10.1177%2F1748301815618299.

Toutin, T., 2004. Review article: Geometric processing of remote sensing images: models, algorithms and methods. Int. J. Remote Sens. 25 (10), 1893–1924. https://doi.org/10.1080/0143116031000101611.

Tschudi, M.A., Maslanik, J.A., Perovich, D.K., 2008. Derivation of melt pond coverage on Arctic sea ice using MODIS observations. Remote Sens. Environ. 112 (5), 2605–2614. https://doi.org/10.1016/j.rse.2007.12.009.

Turner, D., Lucieer, A., Watson, C., 2012. An automated technique for generating georectified mosaics from ultra-high resolution unmanned aerial vehicle (UAV) Imagery, based on structure from motion (SfM) point clouds. Remote Sens. 4 (5), 1392–1410. https://doi.org/10.3390/rs4051392.

Turner, D., Lucieer, A., Wallace, L., 2014. Direct georeferencing of ultrahigh-resolution UAV imagery. IEEE Trans. Geosci. Remote Sens. 52 (5), 2738–2745. https://doi.org/10.1109/TGRS.2013.2265295.

Vihma, T., 2014. Effect of Arctic sea-ice decline on weather and climate: a review. Surv. Geophys. 35, 1175–1214. https://doi.org/10.1007/s10712-014-9284-0.

Vinnikov, K.Y., 1999. Global warming and northern hemisphere sea ice extent. Science 286 (5446), 1934–1937. https://doi.org/10.1126/science.286.5446.1934.

Veksler, O., 2003. Fast variable window for stereo correspondence using integral images. In: Proc. IEEE Computer Society Conference on Computer Vision and Pattern Recognition, Madison, USA, 18–20 June. pp. I–I. doi: 10.1109/CVPR.2003.1211403.

Wu, W., Zhu, H., Yu, S., Shi, J., 2019. Stereo matching with fusing adaptive support weights. IEEE Access 7, 61960–61974. https://doi.org/10.1109/ACCESS.2019.2916035.

Yang, Q., Wang, L., Yang, R., Stewenius, H., Nister, D., 2009. Stereo matching with color-weighted correlation, hierarchical belief propagation, and occlusion handling. IEEE Trans. Pattern Anal. Mach. Intell. 31 (3), 492–504. https://doi.org/10.1109/TPAMI.2008.99.

Yitayew, T.G., Dierking, W., Divine, D.V., Eltoft, T., Ferro-Famil, L., Rosel, A., Negrel, J., 2018. Validation of sea-ice topographic heights derived from TanDEM-X interferometric SAR data with results from laser profiler and photogrammetry. IEEE Trans. Geosci. Remote Sens. 56 (11), 1–17. https://doi.org/10.1109/TGRS.2018.2839590.

Yoon, K.J., Kweon, S., 2006. Adaptive support-weight approach for correspondence search. IEEE Trans. Pattern Anal. Mach. Intell. 28 (4), 650–656. https://doi.org/10.1109/TPAMI.2006.70.

Zhang, J., Li, D.-X., Zhang, M., 2010. Fast stereo matching algorithm based on adaptive window. In: Proc. International Conference on Audio, Language and Image Processing, Shanghai, China, 23–25 November. pp. 138–142. doi: 10.1109/ICALIP.2010.5684994.

Zhang, K., Sheng, Y., Wang, M., Fu, S., 2018. An enhanced multi-view vertical line locus matching algorithm of object space ground primitives based on positioning consistency for aerial and space images. ISPRS J. Photogramm. Remote Sens. 139, 241–254. https://doi.org/10.1016/j.isprsjprs.2018.03.017.

Zhang, Y., Zhang, Y., Mo, D., Zhang, Y., Li, X., 2017. Direct digital surface model generation by semi-global vertical line locus matching. Remote Sens. 9 (3), 214. https://doi.org/10.3390/rs9030214.